Microphase Separation in Star Block Copolymers of Styrene and Isoprene. Theory, Experiment, and Simulation

G. Floudas,*,† S. Pispas,‡,† N. Hadjichristidis,‡,† T. Pakula,§ and I. Erukhimovich⊥

Foundation for Research and Technology−Hellas (FORTH), Institute of Electronic Structure and Laser, P.O. Box 1527, 711 10 Heraklion, Crete, Greece; Department of Chemistry, University of Athens, Panepistimiopolis, Zografou 15771, Athens, Greece; Max-Planck-Institut für Polymerforschung, Postfach 3148, D-55021 Mainz, FRG; and Department of Physics, Moscow State University, Moscow 117234, Russia

Received November 28, 1995; Revised Manuscript Received March 1, 1996[⊗]

ABSTRACT: The order−disorder transition (ODT) and the ordering kinetics have been studied in four-arm star diblock copolymer melts of styrene (corona) and isoprene (core) by rheology and SAXS. The results are compared with the corresponding linear diblock and show that the transition shifts in the direction predicted by theory. The mean-field structure factor is used to describe the SAXS profiles at $T \gg T_{ODT}$ and to extract the temperature dependence of the interaction parameter $\chi(T)$. Because of the weak T dependence of χ, we can explore only a small region of the phase diagram, namely, $16.5 < \chi N_0 < 14.6$, for $f_{PS} = 0.25$. The microphase-separated state consists of spherical microdomains of the minor component (PS) which resembles a bcc phase, however, not with the full symmetry. To explore the morphology over a broader T range, we use the results of computer simulation on equivalent chains, which for $f_{PS} = 0.25$ provide the following succession of phases: hexagonal − a bicontinuous structure which resembles the gyroid − body-centered cubic (bcc) − disordered. The existence of a stable gyroid phase—over a limited composition range—is also predicted by a theory based on a calculation of the higher harmonics. Fluctuation corrected phase diagrams for four-arm star block copolymers are presented here, for the first time. The ordering kinetics have been studied by rheology and show a dramatic slowing of the ordering process as compared to symmetric and asymmetric linear diblocks as a result of the molecular topology and constrained mobility of chains.

Introduction

In the classical picture,[1] the phase behavior of linear diblock copolymers depends on only two parameters: the composition $f = N_A/N$, where $N = N_A + N_B$ is the total number of segments and the reduced interaction parameter χN. In this picture and for $f \neq 0.5$, three ordered morphologies are expected to change from one another via first-order phase transitions with increasing χ (decreasing temperature) in the following order: Dis (disordered phase), bcc (body centered cubic lattice), Hex (planar hexagonal or cylinder phase), and Lam (one-dimensional lamellar structure). All phase transition lines have a common critical (ODT) point at $f = 0.5$, where the only second-order phase transition from Dis−Lam is expected.

Fluctuation effects[2] and polydispersity[3] as well as the contribution of the so-called higher harmonics[3,4] affect both the value of χN at the phase transition lines and the morphology. Fluctuation effects result in the destruction of the less stable phases (first, the bcc phase disappears and the hexagonal phase sometimes as well) and shift the phase transition lines to lower temperatures. In particular, for symmetric diblock copolymer melts we have

$$\chi N_{ODT} = 10.5 + 41(u/\alpha^3)^{2/3}\bar{N}^{-1/3} \qquad (1)$$

where u is the statistical volume and α the Kuhn segment length which is assumed to be the same for monomers A and B. Consequently, the mean-field second-order transition becomes first order. The effect of the higher harmonics is to increase the stability of more symmetric and complex lattices having larger values of the vectors pertaining to the first coordination sphere of the corresponding inverse lattice (see ref 3 and below). It is this effect which is responsible for the observation of nonclassical phases such as hexagonally perforated layers and the bicontinuous (or gyroid) structures. The latter structure was found in both linear[5] and star diblock[6] copolymers and differs from the ordered bicontinuous double-diamond (OBDD) structure. Finally, the conformational asymmetry—differences of the Kuhn lengths and possibly statistical volumes—of the A and B units and the polydispersity, result in the distortion of the phase diagram.[3,7]

The theory of microphase separation has recently been extended to include triblock, graft, and star copolymers.[8−13] In our previous experimental work[14] we studied the case of model graft copolymers of styrene and isoprene and of 3-miktoarm star terpolymers of styrene, isoprene, and butadiene with respect to the microphase separation. We found that the mean-field theory (MFT) can describe the scattering profiles only at temperatures $T \gg T_{ODT}$ and provided evidence for fluctuations near the T_{ODT}. As with the graft copolymers, the $(AB)_n$ star copolymers, where n is the number of arms, do not have a critical point at any f, i.e., all transitions are first order. According to the MFT,[9] a lowering of the transition entropy is expected in the case of star diblocks because of the junction constraint. The transition entropy change for a star diblock is proportional to[9]

$$\Delta S_0 - [(n-1)/n]\ln(1/f) \qquad (2)$$

where ΔS_0 refers to the transition entropy change in

† FORTH.
‡ University of Athens.
§ Max-Planck-Institut für Polymerforschung.
⊥ Moscow State University.
⊗ Abstract published in *Advance ACS Abstracts,* May 1, 1996.

S0024-9297(95)01762-1 CCC: $12.00 © 1996 American Chemical Society

the case of a diblock. Since $(\chi N)_0$ is proportional to the transition entropy, the expectation is that the spinodal will be smaller than for a diblock copolymer. According to the MFT, for $f = 0.5$, $(\chi N)_0$ equals 10.5, 8.86, and 7.07 for $n = 1$, 2, and 4, respectively. Moreover, the spinodal curves are expected to be more asymmetric (see eq 2) than in diblock copolymers, and **Q***, the scattering vector of maximum intensity, goes through a minimum as the composition of the copolymer changes.[9−11] Motivated by the theoretical predictions there have been two investigations of star diblocks by scattering experiments. In the first study,[15] a series of 18-arm star diblocks of styrene and isoprene with different compositions have been used to account for the **Q*** dependence. In the second study,[16,17] a series of asymmetric star diblock copolymers of sytrene and isoprene with n in the range 3−18 have been used. The SAXS profiles were analyzed by the MFT for star diblocks, and quantitative agreement was found. Moreover, the analysis has shown a strong n dependence of the interaction parameter.

In the scattering studies above, the arm molecular weight was more than 30 000, which excluded the possibility of having an experimentally accessible order−disorder transition temperature. In the present study, we use star diblocks of smaller molecular weights with an accessible ODT in the melt state. We use rheology and SAXS to identify the ODT and all the associated features. Rheology has been used earlier in nonlinear block copolymers: graft copolymers of styrene and isoprene and in three miktoarm star terpolymers of styrene, isoprene, and butadiene,[14] as well as in a six-arm star polystyrene−polybutadiene star block copolymer[18] and in polyisoprene−polystyrene miktoarm copolymers of the A_2B_2 type.[19] The ordering kinetics have been studied by rheology and show a dramatic slowing of the ordering process as compared to symmetric and asymmetric linear diblocks. We complement the experimental work with the calculated phase diagrams and with computer simulations on four-arm star diblock copolymers. The former provide the phase diagram in four different representations: (a) mean-field type with and without fluctuation corrections and (b) phase diagrams with the inclusion of higher harmonics with and without fluctuation corrections. In the simulation, the morphology has been identified over a very broad temperature range which is not accessible in the experiments. The work is organized as follows: The phase diagram for a four-arm star diblock copolymer in the different representations is calculated first and experimental results on the morphology and on the process of microphase separation are then presented. The ordering kinetics, as studied by rheology, are discussed next, and in the final section the results from the computer simulations for symmetric and asymmetric star diblock copolymers are shown over a broad T range.

Experimental Section

Samples. The styrene−isoprene four-arm star block copolymers were prepared by anionic polymerization. All reagents (solvents, monomers, and coupling and terminated agents) were purified using standard high-vacuum techniques.[20] Reactions were carried out in all-glass vacuum-sealed, *n*-BuLi-washed, and benzene-rinsed vessels. Benzene was the solvent, and *s*-BuLi the initiator. Styrene was polymerized first followed by the addition of isoprene. The living diblock chains were coupled with tetrachlorosilane, giving the desired four-arm star diblocks. Excess diblock chains, after deactivation with degassed methanol, were separated from the stars by fractionation in toluene using methonal as the nonsolvent. The samples were stabilized with 2,6-di-*tert*-butyl-*p*-cresol and dried under vacuum.

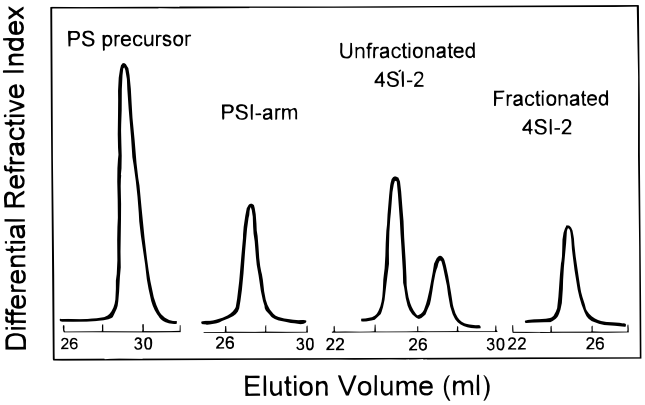

Figure 1. SEC chromatogram of the precursor PSI arm unfractionated and fractionated four-arm star block copolymer 4SI-2.

Table 1. Molecular Characteristics of the Star Block Copolymers and of the Linear Diblock AS25

sample	$\bar{M}_{n,SI}$ (g/mol)	$\bar{M}_{n,PS}$[b] (g/mol)	$\bar{M}_{n,Star}$[a] (g/mol)	w_{PS} (%)[c]	N_0^{arm}	f_{PS}	$(\chi N_0)_{T=293K}$[d]
4SI-1	4 800[b]	2250	17 000	48	58	0.43	3.3
4SI-2	4 300[b]	1200	16 500	27	53	0.25	3.0
4SI-3	24 000[a]	7000	98 000	28	296	0.25	16.7
AS25	23 800[a]	6000		25	295	0.22	

[a] Membrane osmometry in toluene at 37 °C. [b] Vapor pressure osmometry in benzene at 40 °C. [c] ^{1}H NMR in $CDCl_3$ at 30 °C (note: by SEC-UV on the diblock arms: 4SI-1: 47 wt % PS, 4SI-2: 26 wt % PS, 4SI-3: 29 wt % PS). [d] Calculated using $\chi = 0.034 + 6.6/T$ (see text).

At each step of the synthesis, the samples were isolated from the reactors by sealing off the appropriate constrictions, for characterization of the intermediate products (first block and diblock arm) as well as to follow the course of the coupling reaction. SEC was used primarily for this purpose (see, for example, Figure 1), yielding also the polydispersity indexes ($\bar{M}_w/\bar{M}_n$) of the products, which was less than 1.1 in all cases. The molecular weights of the PS precursor, the diblock arm and the fractionated stars were measured by membrane and vapor pressure osmometry ($\bar{M}_n$) and with low-angle laser light scattering ($\bar{M}_w$). The styrene content was determined by ^{1}H NMR. The procedures followed are described elsewhere[21] in more detail. The characteristics of the three star diblock copolymers and of the asymmetric linear diblock are shown in Table 1.

Rheology. The storage and loss moduli G' and G'' have been measured using two rheometers: a Rheometrics RMS 800 and a Rheometric Scientific dynamic stress rheometer (DSR). Both rheometers were used in the oscillatory mode with a parallel-plate sample geometry. The sample temperature was controlled with a nitrogen gas in the former, whereas the heated plates of the latter rheometer were found to be more suitable for the kinetic studies (see below). Different types of experiments have been performed using the two rheometers. First, the linear and nonlinear viscoelastic ranges were identified from the strain dependence of the complex shear modulus G^* $(=(G'^2 + G''^2)^{1/2}$; inset to Figure 2). The dependence of G^* on the strain amplitude is shown in the inset to Figure 2 for two frequencies, and the two viscoelastic ranges are separated by arrows. Strain amplitudes above the critical ones have been used in order to induce orientational order in the material. Figure 2 shows the time evolution of G^* for the star diblock 4SI-3 which is shear oriented at $T =$ 403 K (a temperature located above the PS glass transition temperature, T_g, but below the T_{ODT}) with a strain amplitude of 50% and at a frequency of 10 rad/s. Under such conditions the specimen can be oriented on a macroscopic scale. Evidence for the induced orientation comes from the shape of $G^*(t)$ which is a decreasing function of time. The decrease of $G^*(t)$ during

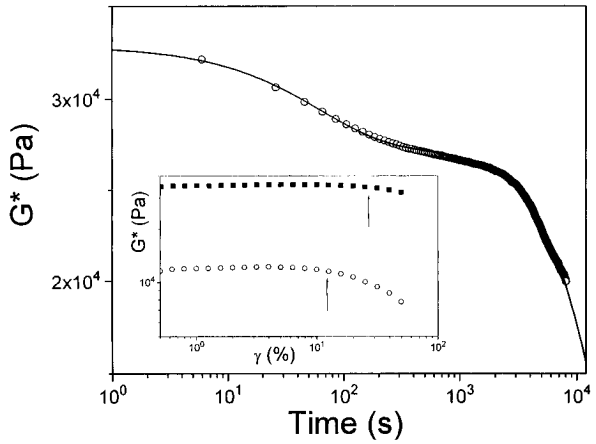

Figure 2. Time evolution of the complex shear modulus of 4SI-3 during an isochronal/isothermal scan at $T = 403$ K. The frequency was 10 rad/s, and the strain amplitude 50% (nonlinear viscoelastic range). The inset gives the strain dependence of G^* at two frequencies, and the vertical arrows separate the linear and the nonlinear viscoelastic range.

orientation has been attributed to the elimination of interfaces perpendicular to the shear direction which can be accomplished by the reorientation of the domains along the shear direction.[22] The shape of $G^*(t)$ depends largely on the conditions and of the system. In general, linear diblock copolymers show a single and continuous drop of $G^*(t)$ which is more stretched than a single-exponential decay.[23] For the star diblock copolymers, as well as for the earlier investigated graft and star terpolymers,[14] the shape of the $G^*(t)$ resembles the well-known Kohlrausch−Williams−Watts (KWW) function:

$$G^*(t) = \sum_i \Delta G_i^* \exp[-(t/\tau)^{\beta_i}] \qquad (3)$$

where ΔG^*, τ, and β_i are the amplitude of the modulus relaxation, the relaxation time, and the shape parameter, respectively. The two step relaxation shown in Figure 2 can be fitted with shape parameters: $\beta_1 = 0.8$, $\beta_2 \approx 1$ and with a characteristic time ratio of $\tau_1/\tau_2 = 3.5 \times 10^{-3}$. Although there is little knowledge of the possible origin of the two processes, we can speculate domain reorientation along the shear direction followed by a perfection of the structure as the possible mechanisms. The oriented sample was subsequently quenched to temperatures below the polystyrene T_g and studied by SAXS.

In the remaining studies we have performed different experiments using low strain amplitudes (well within the linear viscoelastic range). The first such experiment consisted of isochronal temperature scans (at $\omega = 1$ rad/s) by heating the star and linear diblocks aiming to identify the order−disorder transition. Isothermal frequency scans were performed above and below the T_{ODT} aiming to construct the master curves by making use of the time−temperature superposition principle. Last, isothermal/isochronal scans (at $\omega = 1$ rad/s) were made for the linear diblock AS25 and for the star diblock 4SI-3 following a quench from the disordered phase aiming to unravel and compare the ordering kinetics. To avoid sample decomposition at the elevated temperatures used for the kinetic studies, measurements were performed in an inert atmosphere.

Small-Angle X-ray Scattering. Two SAXS setups have been used. In the first one the source was an 18 kW rotating anode (Rigaku) with a pinhole collimation and a two-dimensional detector (Siemens) with 512 × 512 pixels. A double graphite monochromator for the Cu Kα radiation ($\lambda = 0.154$ nm) was used. The beam diameter was about 1 mm, and the evacuated sample-to-detector path was 1.2 m. The three possible sample orientations (normal, tangential, and radial) were investigated at ambient temperature, and the T dependence of the SAXS patterns was investigated for the radial direction. Since in that experiment we are mainly

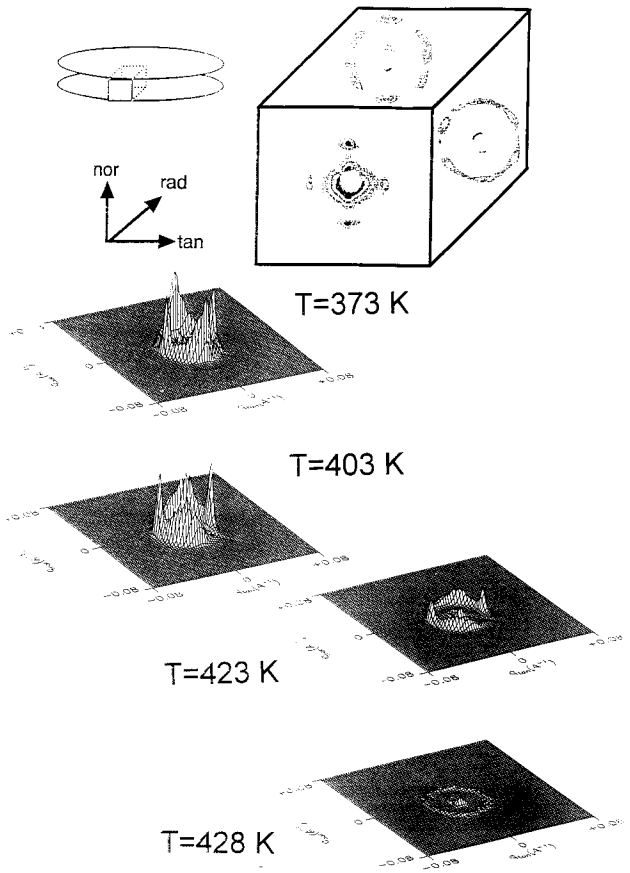

Figure 3. Top: SAXS patterns of the 4SI-3 star diblock copolymer taken with the 2-dimensional detector at $T = 300$ K. The tangential, normal, and radial views are shown together with the coordinate system. Bottom: effect of heating the sample in the radial view. The sample disorders at $T_{ODT} = 428$ K.

interested on the morphology of the oriented sample, the intensities are given in arbitrary units; however, care was taken in using samples with equal thickness in all three orientations. The SAXS profiles were taken from a point where the strain amplitude was 30%.

The second setup was the familiar Kratky−Compact camera (Anton Paar KG) equipped with a one-dimensional position-sensitive detector which is more suitable for the quantitative analysis of the scattering profiles. Measurements of 1 h long were made at intervals of 5 K within the range 298−453 K with a stability better than ±0.2 K. The smeared intensity data were collected in a multichannel analyzer and were subsequently corrected for absorption, background scattering, and slit-length smearing using the procedure described elsewhere.[24] Primary beam intensities were determined in absolute units by using the moving slit method.

Morphology. From the three star diblock copolymers investigated only the sample 4SI-3 undergoes an order−disorder transition within the accessible T range. The sample was shear oriented (Figure 2) and examined with the two-dimensional detector. The X-ray patterns for the tangential, normal, and radial directions are shown in Figure 3. In Figure 3 the effect of heating the sample to 428 K for the radial direction is also shown. At temperatures below 423 K, the spots in the radial direction possess a 4-fold symmetry, which would imply spherical microdomains of the minority component (PS) organized in a bcc lattice. However, the normal and tangential views possess a 6-fold symmetry. It is worth noticing that the temperature interval 303−428 K corresponds to the reduced interaction parameter range 16.5−14.6, where, according to the mean-field predictions a bcc lattice is expected (see below). The sample disorders at a temperature in the range 423−428 K as evidenced by the isotropic scattering and the corresponding χN_0 value is about 14.6, in accord with the

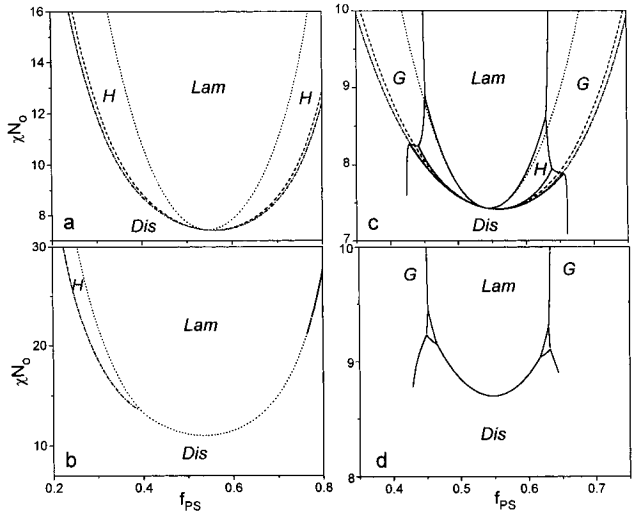

Figure 4. Calculated phase diagram for star block copolymers. (a) Conventional mean-field type phase diagram showing the Dis−bcc (dash−dotted), bcc−Hex (dashed), and Hex−Lam (dotted) phase transition lines. (b) Typical phase diagram calculated with fluctuation corrections (the value of the perturbation parameter $z = 0.475$) but without higher harmonics. The region of the bcc phase is completely destroyed and the region of the hexagonal phase for high values of the composition f is so narrow that the Dis−Hex and Hex−Lam phase transition lines are nearly merged (solid line). (c) Mean-field type phase diagram calculated with the higher harmonics' effect showing the presence of the new gyroid phase. The lamellar, hexagonal, bcc and the gyroid phases are separated by solid lines, and the results corresponding to Figure 4a are also shown for comparison (dashed lines). (d) A typical phase diagram calculated allowing for both fluctuations (the value of $z = 0.1$) and higher harmonic effects. The regions of the bcc phase are completely destroyed by fluctuations and only small islands of the hexagonal phase have survived between large regions of lamellar, disordered, and gyroid phases.

MFT predictions. As expected, the use of the χ parameter which has been extracted from the MFT (see below) gives results consistent with the theoretical expectation for χN_0, at the ODT.

Results and Discussion

Calculation of Phase Diagrams. The physical nature of the process of microphase separation in block copolymer systems is understood now sufficiently well. From the point of view of the Landau phase transition theory a system under microphase separation undergoes a set of phase transitions that can be described in terms of the vector order parameter:

$$\Phi_\alpha(r) = \rho_\alpha(r) - \bar{\rho}_\alpha \tag{4}$$

where ρ_α is the local density of monomers of type α (i.e., the number of monomers in a unit volume) and $\bar{\rho}_\alpha$ is an average value of the density over the volume V of the system.

All components of the order parameter are equal to zero in the high-temperature homogeneous (disordered) phase. However, with decreasing temperature T the order parameter becomes a function of coordinates having the symmetry of a Bravais lattice:

$$\Phi_\alpha(r) = \sum_{\{q_i\}} A(q_i)\exp(iq_i r) \tag{5}$$

where the summation is over all vectors of the corresponding inverse lattice. A change of T leads first to a continuous increase of the amplitudes ($A(q_i)$ in eq 5), and, at a certain transition temperature, to a discrete change of symmetry. Similarly, a change in the composition f results in continuous changes in the interval between two transition lines and to a discrete change on the transition line itself.

The phase diagrams for star diblock melts of the type $(AB)_n$ have been calculated for $n = 2$ (symmetric triblocks[10,12,13]) and for $n = 5$, 10[13,25] following the classical weak crystallization approach.[26,27] This approach was advanced after realizing (first by Leibler[1] and de Gennes[28] and independently by one of the authors[29]) that the microphase separation of a heteropolymer is caused by an instability of its homogeneous state with respect to spatial composition fluctuations of a finite period L_c. Since these are the fluctuations which dominate the initial state of domain structure formation, it is expected that near the ODT only the plane waves of the most dangerous length L_c in the sum of eq 5 are important. Therefore one writes

$$\Phi_\alpha(r) = \sum_{\{q_i=q^*\}} A(q_i)\exp(iq_i r) \tag{6}$$

where q^* ($=2\pi/L_c$) is assumed usually to be the radius of the first coordination sphere of the corresponding Bravais lattice. This assumption enables to express the free energy of the system as a Landau expansion on the amplitudes $A_i = A(q_i)$:

$$F = F_0 + \min \Delta F$$

$$\frac{\Delta F}{VT} = \frac{1}{2}\sum_{\{q_i\}} \gamma^{(2)}(q_i)|A_i|^2 + \frac{1}{3!}\sum_{q_i+q_j+q_k=0} \gamma^{(3)}(q_i,q_j,q_k)A_iA_jA_k + \frac{1}{4!}\sum_{q_i+q_j+q_k+q_l=0} \gamma^{(4)}(q_i,q_j,q_k,q_l)A_iA_jA_kA_l \tag{7}$$

where F_0 is the free energy of the spatially homogeneous state. The coefficients $\gamma^{(i)}$ are expressed in terms of the so-called higher structural characteristics of macromolecules.[1,10,12,13,25] The coefficient $\gamma^{(2)}$ for star diblocks was calculated first in ref 9. It can be shown that all moduli of the equilibrium amplitudes A_i are equal to the same value A, resulting in the following expression for ΔF:

$$\Delta F = \min\left(\frac{\tau A^2}{2} + \frac{\alpha_\kappa A^3}{6} + \frac{\beta_\kappa A^4}{24}\right) \tag{8}$$

The index κ in eq 8 corresponds to the different lattices, and 2κ is just the number of vectors which belong to the first coordination sphere of the corresponding inverse lattice. The value of the minimum in eq 8 should be searched in the limits ($-\infty < A < \infty$) and α_κ, β_κ, τ are certain functions of f and the number of arms n (τ also depends on χN).

The calculated phase diagram for star diblocks $(AB)_n$ with $n = 4$, in the context of the mean-field approximation using the expressions for higher correlators,[13] is shown in Figure 4a. The general behavior of the curves $\chi N(f)$ resemble the spinodals of ref 9 showing the conventional succession of phase transitions: Dis−bcc−Hex−Lam. The fluctuation corrections to the phase diagram can be calculated within the framework of the Brazovskii−Fredrickson−Helfand approach[2,30−34] and result in the phase diagram shown in Figure 4b. The

fluctuation corrections shown in Figure 4b, correspond to the following value of the perturbation parameter: $z = (u/a^3)(6^{3/2}/N_0^{1/2}) = 0.475$. Fluctuations result in the destruction of the less-stable phases. This effect is more prominent for the bcc phase but expands also to the hexagonal phase (such corrections were calculated for $n = 2$ and $n = 5$, 10 in refs 32−34 and 32, respectively).

Note that neither the phase with bitetrahedral (OBDD) symmetry nor one with the gyroid symmetry is present in Figure 4a,b. The reason is that the structures of the first coordination spheres of the OBDD and bcc lattices are the same.[35] Therefore, within the framework of the conventional version of the weak crystallization theory—which takes into account only vectors of the first coordination sphere in the sum of eq 5—it is impossible to differentiate between them. The investigation of the existence of e.g., the gyroid phase, requires the presence of the higher harmonics, that is, the plane waves with wave vectors q_i pertaining to the second and higher coordination spheres.

The problem was addressed first in refs 4 and 36. It was shown there that the contribution from higher harmonics results in the appearence of some new phases which are different from the classical Lam, Hex, and bcc phases. In ref 3, it was shown that within the framework of a proper extension of the weak crystallization theory, only those higher harmonics are relevant which correspond to the inverse lattice vectors resulting from the sum of only two vectors pertaining to the first coordination sphere. Indeed, assuming that the higher harmonic amplitudes are smaller than the first ones (which is natural within the weak crystallization limit) the free energy can be generalized as follows:

$$\Delta F = \Delta F_0 + \Delta F_{hh}$$

$$\Delta F_{hh} = \sum_{q_i^p} \gamma^{(2)}(|q_i^p|) \frac{A(q_i^p)\, A(-q_i^p)}{2} + \sum_{q_i^1 + q_j^1 + q_k^p = 0} \gamma^{(3)}(q_i^1, q_j^1, q_k^p) \frac{A(q_i^1)\, A(q_j^1)\, A(q_k^p)}{2} \quad (9)$$

where ΔF_0 is defined by eq 7, and the summation in the quadratic term is over all higher harmonics, i.e., those vectors q_i^p of the inverse lattice which do not belong to the first coordination sphere. The cubic term is linear with respect to the higher harmonic amplitudes and bilinear with respect to the first one.

The minimization of ΔF_{hh} with respect to the higher harmonic amplitudes $A(q_k^p)$ results in the following bilinear dependence of their equilibrium values on the values of the first harmonic amplitudes $A(q_k^1)$:

$$A(q_\kappa^p) = -\sum \gamma^{(3)}(q_i^1, q_j^1, q_k^p) \frac{\tilde{A}(q_i^1)\, \tilde{A}(q_j^1)}{\gamma^{(2)}(|q^p|)} \quad (10)$$

where the wave vectors q_i^1 and q_j^1 are related to the wave vectors q_k^p of the higher harmonics via the condition

$$q_i^1 + q_j^1 + q_k^p = 0 \quad (11)$$

It follows from the above equation that only those higher harmonics q_k^p for which eq 11 is fulfilled for any choice of the first harmonics q_i^1 and q_j^1 contribute to the free energy. Substitution of the expression for $A(q_k^p)$ of eq 10 into 9, results in the following correction to the free energy:

$$\Delta F_{hh}(\tilde{A}(q_i^1)) = -\sum_{q_i^1, q_k^1, q_l^p, p>1} \frac{(\gamma^{(3)}(q_i^1, q_j^1, q_k^p))^2}{8\gamma^{(2)}(|q^p|)} \times A(q_i^1)\, A(q_l^p - q_i^1)\, A(q_k^1)\, A(-q_k^1 - q_l^p) \quad (12)$$

This correction is always negative since the introduction of new adjustable parameters—the higher harmonics' amplitudes—can only decrease the total free energy of the system and the correction is proportional to the fourth power of $A(q_i^1)$. In other words, the effect of the higher harmonics is equivalent to a renormalization (decrease) of the effective coefficient β_κ in eq 8. The effect is more pronounced the larger is the modulus of the coefficient $\gamma^{(3)}$ (i.e., the further away the system is from its critical point). Moreover, further increase in the value of $|\gamma^{(3)}|$ may cause a change of sign from a positive β_κ to a negative one ($\tilde{\beta}_\kappa$) which would imply that the system cannot be regarded as weakly segregated any more.

Recently this approach was extended to include the possible existence of the gyroid phase.[37] The corresponding calculations allow for the competition of nine phases: disordered, lamellar, simple square, simple cubic, fcc, hexagonal, bcc, quasicrystal, and gyroid. The simple square phase corresponds to cylinders arranged on a square lattice, and the quasicrystal phase is described by a set of plane waves with the corresponding wave vectors forming an icosahedron. The result of the phase competition is shown in the phase diagram of Figure 4c. The fcc, simple cubic, simple square, and quasicrystals phases were never found to be more stable than the bcc, Lam, Hex, gyroid, and disordered phases. The presence of the term ΔF_{hh} results in the following dramatic changes of the conventional Leibler-like phase diagram shown in Figure 4a:

(i) The lines $\chi N_0(f)$ corresponding to the transitions: Dis−bcc, bcc−Hex, and Hex−Lam terminate on a completely new line, delineating the region where the gyroid phase (G) exists. Additionally, three triple points appear (G−Lam−Hex, G−Hex−bcc, and G−bcc−Dis).

(ii) The phase transition lines $\chi N_{0,G-Lam}(f)$ grow with vertical asymptotes at values of f satisfying the condition: $\beta_{Lam}(f) = \beta_G(f)$.

(iii) The phase transition lines $\chi N_{0,G-bcc}(f)$ drop with vertical asymptotes at values of f satisfying the condition: $\beta_G(f_{lim}) = 0$.

Notice that excluding the gyroid phase from the list of competing phases would result in a similar phase diagram where the new phase delineated by the curves with the vertical asymptotes would be the quasicrystal (icosahedral) phase. The detailed discussion of the relationship between the above conditions and the general outlook of the phase diagram obtained with the inclusion of the higher harmonics was presented first in ref 3. There the competition of only eight phases (disordered, lamellar, simple square, simple cubic, fcc, hexagonal, bcc, and quasicrystal) was assumed.

The gyroid phase proved to be the phase with the lowest free energy in the region between the two asymptotes, but for f below this limit the system cannot be regarded as weakly segregated anymore, and we cannot make any prediction for phases outside the composition range shown in Figure 4c. We conclude that the renormalization of the effective coefficient $\tilde{\beta}$ and

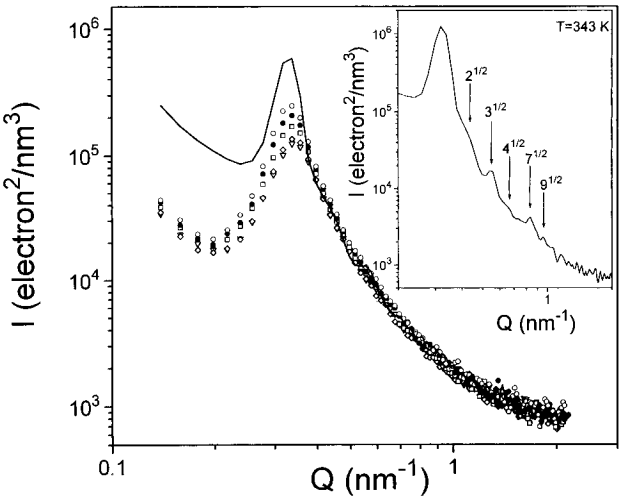

Figure 5. SAXS intensity profiles for the 4SI-3 star diblock at different temperatures: (—) 423, (○) 433, (●) 438, (□) 443, (◇) 448 and (▽) 453 K. The inset gives the scattering pattern in the ordered phase (T = 343 K).

the fact that this coefficient vanishes at $f = f_{lim}$ for the gyroid phase, plays a key role in the general outlook of the phase diagram. Furthermore, fluctuation corrections vanish together with the effective coefficient $\tilde{\beta}$, so that they can affect only the intermediate bcc and Hex phases but not the gyroid phase near f_{lim}. A typical phase diagram demonstrating the effect of fluctuation corrections is shown in Figure 4d.

It is worthwhile, at this point, to compare the phase diagrams of Figure 4c,d with those presented by Matsen and Schick,[38,39] who first predicted the gyroid phase theoretically. They also found the triple points G—Lam—Hex having approximately the same location as in our phase diagram shown in Figure 4c. However, the general outlook of their phase diagram resembles more our mean-field phase diagram of Figure 4a, except for the presence of a narrow "semi-island" of the Gyroid phase between the Lam and Hex phases. Their derivation is based on the expansion of the free energy on certain orthonormal basis functions possessing the symmetry of the phase under consideration. Even though it seems to be very different from the method employed here, their basis functions are in fact related to our higher harmonics, which seems to be the reason for the similarity of the phase diagrams.

SAXS. The SAXS intensity from a two-component system is dominated by the scattering due to concentration fluctuations:

$$I_c = (n_{PS} - n_{PI})^2 VS(Q) \qquad (13)$$

where n_i is the electron number densities of PS and PI and $S(Q)$ is the static structure factor for concentration fluctuations. In addition, there exists scattering due to the density fluctuations which depend on the average electron density $\bar{n}$ and the isothermal compressibility $\beta_T(T)$. Notwithstanding the small contribution to the scattered intensity from the latter mechanism, a reliable subtraction from the former involves a separate measurement of the isothermal compressibility as a function of temperature (i.e., PVT measurements) and subtraction of the calculated contribution at each temperature.[40] Only this procedure provides the scattering spectrum originating from the concentration fluctuations alone. Typical SAXS spectra corrected for the density fluctuations are shown in Figure 5 for the 4SI-3

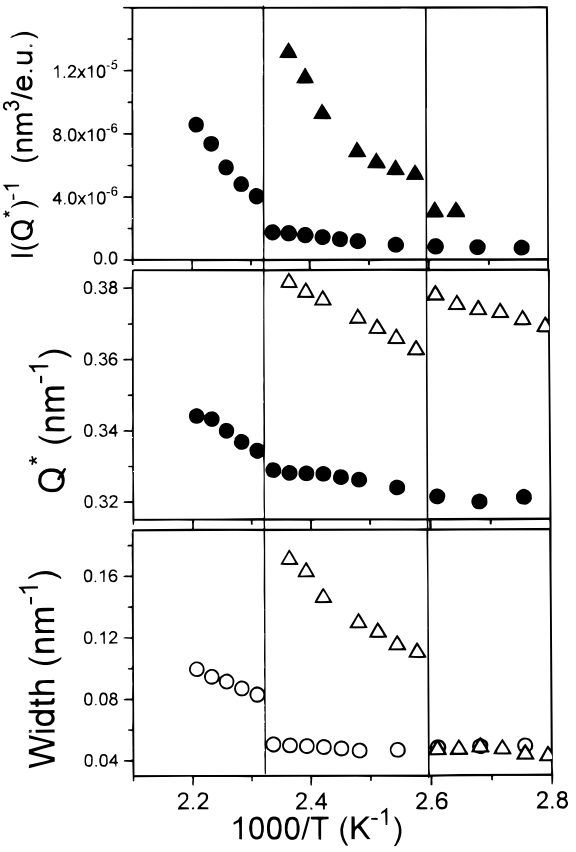

Figure 6. Peak parameters (inverse peak intensity, peak position, and width) plotted vs inverse temperature for the 4SI-3 star diblock (circles) and the AS25 linear diblock (triangles). The two vertical lines indicate the corresponding ODT temperatures.

sample, for different temperatures in the range 428—453 K. As with the two-dimensional SAXS data (Figure 3), there is a change of the scattering pattern at about 428 K which reduces in intensity and becomes isotropic at the ODT. At temperatures below 428 K, the scattering profile is dominated by an intense sharp peak with additional reflections at positions $2^{1/2}$, $3^{1/2}$, $4^{1/2}$, $7^{1/2}$, and $9^{1/2}$ (inset to Figure 5). Such reflections are characteristic of a structure with a cubic symmetry. On the other hand, the first few reflections of the OBDD structure ($Pn\bar{3}m$ space group) are $2^{1/2}$, $3^{1/2}$, $4^{1/2}$, $6^{1/2}$, $8^{1/2}$, $9^{1/2}$, $10^{1/2}$, and $11^{1/2}$ and of the bicontinuous cubic phase with the $Ia\bar{3}d$ space group symmetry (gyroid phase) are $3^{1/2}$, $4^{1/2}$, $7^{1/2}$, $8^{1/2}$, $10^{1/2}$, and $11^{1/2}$. Clearly, the reflections shown in Figure 5 do not correspond to either of the two structures. Additionally, the peak positions have also been identified by radially integrating the two-dimensional patterns. Because of the pinhole collimation used in the latter system, there is no need for desmearing of the SAXS data. At temperatures above the T_{ODT} there is a single albeit broad peak which is slightly shifted to higher Q. All the higher order reflections from $T < T_{ODT}$ disappear at $T > 428$ K. An intriguing feature of the SAXS profiles (Figure 5) for the star diblock 4SI-3 is that the ODT affects the intensities for all Q smaller than Q^*. This can be attributed to a long-range organization of domains with spherical symmetry and/or to the core/shell form factor characterizing the self-micellarization which takes place in star diblock copolymers.

The peak parameters (peak intensity, position, and width) for the star diblock 4SI-3 are plotted in Figure 6 and compared with the ones for the linear diblock AS25

(Table 1). The latter has the same composition and similar molecular weight with the SI arm in the star diblock. For a consistent analysis below and above the ODT we have used a single Lorentzian function to extract the peak parameters. According to the expectations born out from the theory, the asymmetric linear diblock AS25 disorders at a temperature (T_{ODT} = 385 K) which is about 43 K below the corresponding temperature of the star diblock copolymer. The nonlinearity of the $I(Q^*)^{-1}$ vs T^{-1}—which is more pronounced in the AS25—has been discussed in terms of fluctuation effects near the ODT. Furthermore, Q^* for the star diblock copolymer is shifted to smaller Q values as compared to the linear AS25. For star diblocks, the radius of gyration shows a pronounced dependence on the number of arms: the formation of an $(AB)_2$ (i.e., a triblock) from two diblock copolymers doubles the length and for small n the radius of gyration becomes $R^2 = gR_0^2$, where $g = 1 + (2n(n-1)/n)$ and $R_0^2 = N_0a^2/6$. This increase of the dimensions, for small n, will result in the shift of the peak to smaller values. With a further increase in n, the star develops a core-shell type of morphology and shrinks, resulting in the increase of Q^*. Thus, Q^* in the star diblocks is expected to go through a minimum as a function of the number of arms. We have used the unperturbed radius of gyration of PS[41] and PI[42] (R_0^2 = 23.7 nm^2) and the theoretical predictions[9] for the peak positions of the asymmetric linear and star diblock systems ($Q^{*2}R_0^2 = 3.795$ and 3.318, respectively, for $f_{PS} = 0.26$) and obtained Q^* at 0.4 and 0.374 nm^{-1}, respectively. The measured values—at the ODT—are 0.36 and 0.33 nm^{-1}, respectively, and the difference can be understood in terms of chain extension in the disordered phase. The peak position has also a temperature dependence which is not taken into account in the mean-field theory. Below the T_{ODT} there is only a weak T dependence of the Q^* but at $T > T_{ODT}$ there is a stronger T dependence ($T^{0.12}$) which is at variance from the earlier published data[16] on star diblocks. Last, the best identification of the T_{ODT} can be made by the peak width which shows the bigest discontinuity at this temperature.

The structure factor for the concentration fluctuations $S(Q)$ has been calculated in the disordered phase and has the same functional form for all copolymers:

$$\frac{1}{S(Q)} = \frac{F(x_0,f)}{N_0} - 2\chi \tag{14}$$

where $x_0 = (QR_0)^2$ and $F(x_0,f)$ depends strongly on the molecular architecture. For a linear diblock[1]

$$F(x_0,f) = [D(1,x_0)]/[D(f,x_0)\,D(1-f,x_0) - {}^1/_4[D(1,x_0) - D(f,x_0) - D(1-f,x_0)]^2] \tag{15}$$

where

$$D(f,x_0) = \frac{2}{x_0^2}[fx_0 - 1 + e^{-fx_0}] \tag{16}$$

For the n-arm star diblock copolymer considered here, the function $F(x_0,f)$ is given by[9]

$$\{D(f,x_0) + D(1-f,x_0) + (n-1)[C_f^2 + C_{1-f}^2\exp(-2fx_0)] + 2C_fC_{1-f}[1 + (n-1)\exp(-fx_0)]\}/\{D(f,x_0)\,D(1-f,x_0) + (n-1)[D(1-f,x_0)C_f^2 + D(f,x_0)C_{1-f}^2\exp(-2fx_0)] - (C_fC_{1-f})^2[1 + 2(n-1)\exp(-fx_0)]\} \tag{17}$$

where

$$C_f(x_0) = (1 - e^{-fx_0})/x_0 \tag{18}$$

and $N = nN_0$.

The spinodal, $(\chi N_0)_s$, shifts to lower values when compared to diblock copolymers and the spinodal lines become more asymmetric the higher the number of arms. The fits of the MFT to the experimental SAXS profiles are shown in Figure 7 for the star diblock copolymer 4SI-3 and in the inset for the linear diblock AS25. The MFT better fits the profiles for the star rather than for the linear diblock copolymer. For the latter, there are systematic deviations even at the highest temperature investigated ($T = T_{ODT} + 38$ K). Near the ODT the theory fails in describing the star diblock profiles as well. The T dependence of the interaction parameters for the two systems are plotted in Figure 8. For the star diblock this T dependence can be parametrized as $\chi = 0.034 \pm 6.6/T$. This dependence on T is more weak than for the corresponding diblock ($\chi = 0.03 + 10/T$). The calculation of χ is based on the statistical volume $(u_{PS}u_{PI})^{1/2}$ of 144 Å^3. The weak T dependence and the values of the enthalpic and entropic contributions agree with the previously estimated for a four arm star diblock copolymer.[16] The values of χN_0 and χN at the spinodal are 14.6 and 15.6 for the star and linear diblocks, respectively, which is also the expectation from the mean-field theory.

Rheology. All the rheological experiments below have been made with small strain amplitudes (typically below 5%) which correspond to the linear viscoelastic range, in order to avoid the macroscopic orientation of the sample. Isochronal measurements at $\omega = 1$ rad/s have been performed for all four samples of Table 1, and the results are shown in Figure 9 for three of the samples. All the isochronal measurements have been made by heating the samples in order to decouple the kinetic effects which could smear-out the transition.[14,23,24,43] Only for the linear diblock AS25 and for the star diblock 4SI-3 there is a sharp drop of the moduli at a temperature which is in excellent agreement with the T_{ODT} as obtained from SAXS (Figures 3 and 5–7). Again, in agreement with the SAXS results, for the star diblocks with the smaller molecular weight there is no such transition (disordered phase). The construction of a master curve for the storage and loss moduli obtained under isothermal conditions is expected to be more complicated for the two samples which undergo the order–disorder transition.

The results of the attempted time–temperature superposition are shown in Figures 10–12 for the star 4SI-1, the linear diblock AS25, and the star diblock 4SI-3, respectively. A master curve construction was successful only in the former system which is in the homogeneous phase. At low reduced frequencies and at high temperatures, the moduli display typical terminal zone behavior with the expected frequency dependences: $G' \sim \omega^2$ and $G'' \sim \omega$. The shift factors used for the master curve construction are plotted in the inset and the

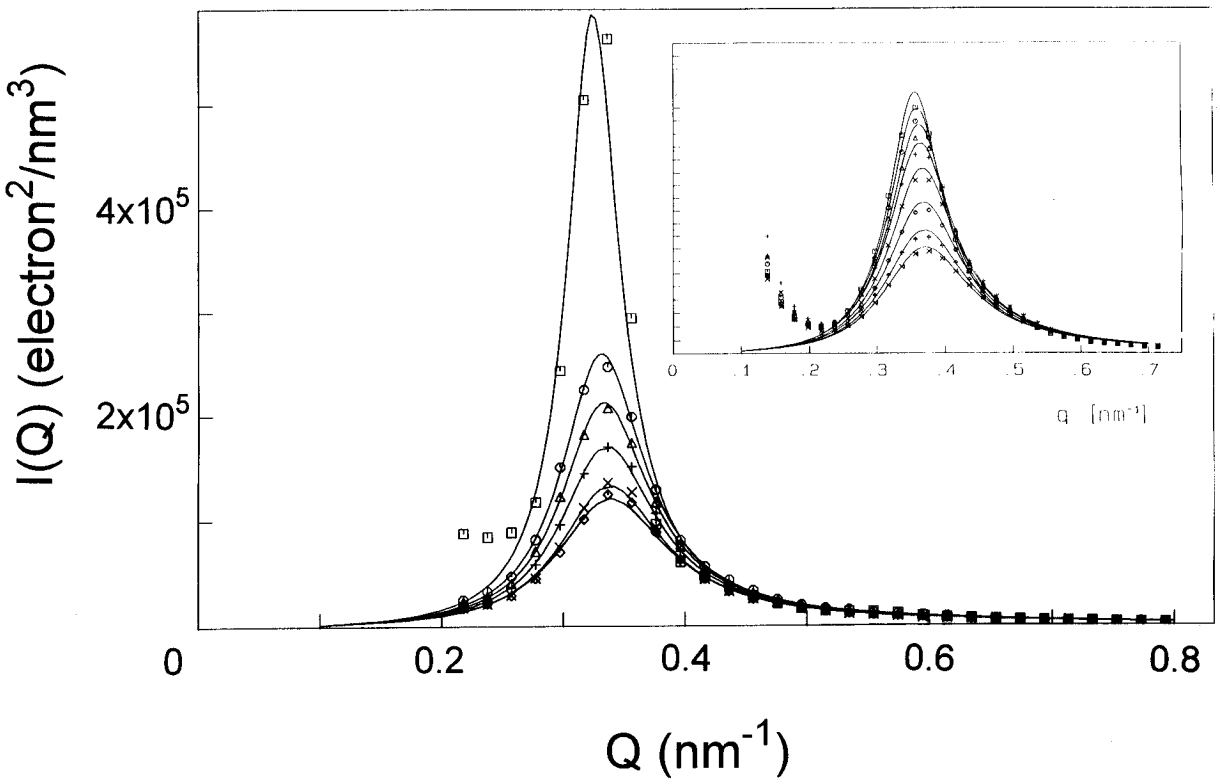

Figure 7. SAXS profiles for the 4SI-3 star diblock at different temperatures: (□) 428, (○) 433, (△) 438, (+) 443, (×) 448, and (◇) 453 K. Solid lines are fits to the MFT for star diblocks. In the inset are the corresponding data and the MFT fits to the asymmetric linear diblock AS25 at temperatures of (□) 388, (○) 393, (△) 398, (+) 403, (×) 408, (◇) 413, (↑) 418, (×) 423 K.

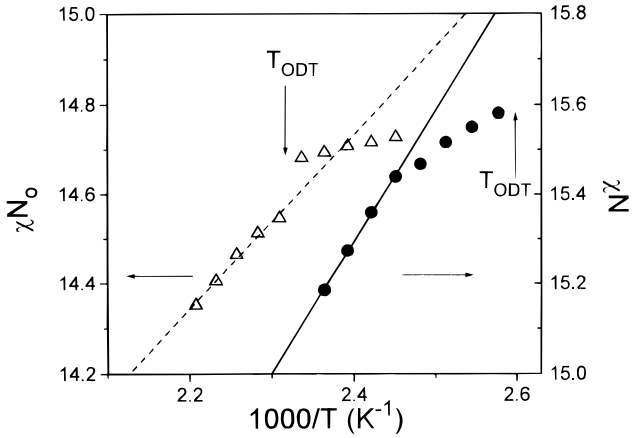

Figure 8. Temperature dependence of χN_0 for the star diblock 4SI-3 and χN for the linear diblock AS25. The ODT temperatures are shown with vertical arrows.

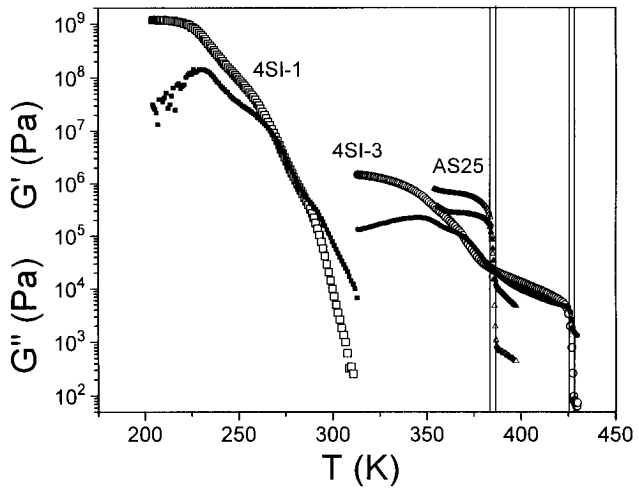

Figure 9. Isochronal measurements of the storage and loss moduli at 1 rad/s. Vertical lines indicate the T_{ODT} for the star diblock 4SI-3 and for the linear diblock AS25. Measurements have been made with as low strain amplitude as possible (typically <5%).

corresponding WLF coefficients are $c_1° = 24$, $c_2° = 206$ K at the reference temperature ($T_0 = 293$ K). For the asymmetric linear diblock there is a pronounced failure of the time−temperature superposition at temperatures below the T_{ODT} (Figure 11). Surprisingly, even the high frequency data *cannot* be superimposed on a single curve and only the low-frequency moduli at $T > T_{ODT}$ can be superimposed with the expected terminal zone-limiting slopes. For the high molecular weight star diblock ($T_{ref} = 383$ K) there is again a failure of the time−temperature superposition for G' and G'' below the frequencies ω_1 and ω_2, respectively (Figure 12). The low-frequency moduli below the T_{ODT} display a limiting slope of about $^1/_3$. It is worth noticing that this slope is intermediate between the predicted ones[44] for a strongly segregated lamellar mesophase ($\omega^{1/2}$) and for a cylindrical mesophase ($\omega^{1/4}$). The non-Newtonian behavior at $T < T_{ODT}$ is attributed to the relaxation of grains which would need much longer times to relax. Evidence for the grain relaxation has recently been provided in block copolymers of other architectures.[45] In conclusion, rheology provides the order−disorder transition with a good accuracy in agreement with the SAXS results. The big separation of the low-frequency Newtonian ($T > T_{ODT}$) and non-Newtonian ($T < T_{ODT}$) behavior, which depends on the frequency, provides the means of exploring the ordering kinetics.

Ordering Kinetics. Rheology has been established as the main tool in studying the ordering kinetics in diblock copolymers.[14,23,24,46] The reason is the large dynamic separation of the shifted moduli at low frequencies; thus by choosing a frequency below ω_1 and

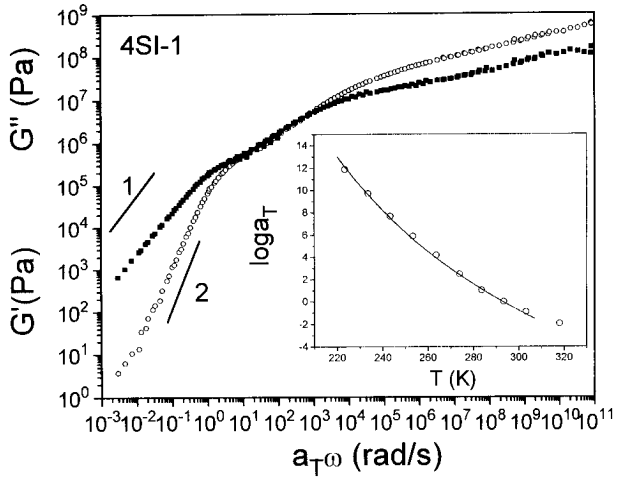

Figure 10. Reduced frequency plot for G' and G'' of the star diblock copolymer 4SI-1. The reference temperature was 293 K. The shift factors are plotted in the inset.

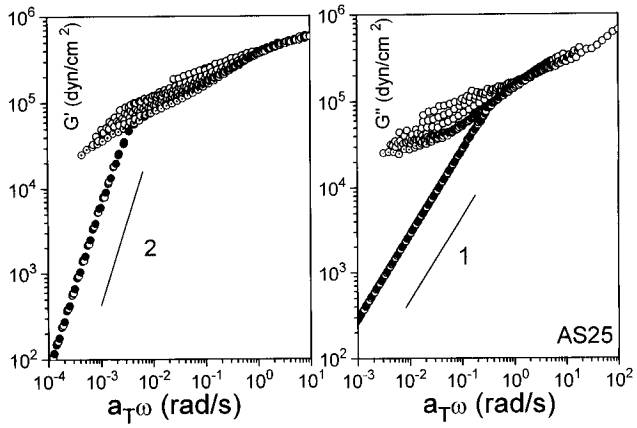

Figure 11. Reduced frequency plot for the G' and G'' of the asymmetric linear diblock AS25 at two selected temperatures: (●) T = 385 K and (⊙) T = 382 K. The reference temperature was 338 K, and the stain amplitude was 2%. The corresponding limiting slopes at low frequencies are shown.

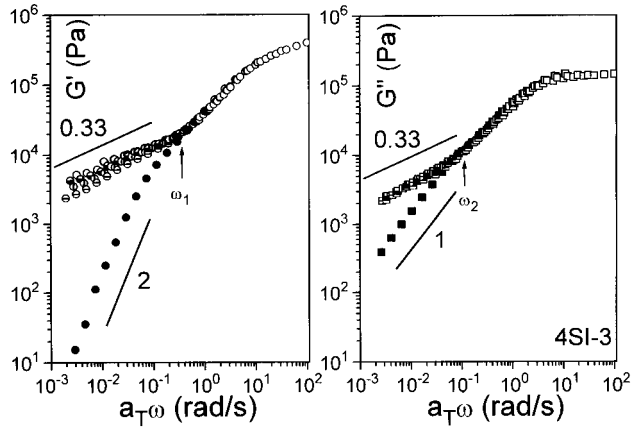

Figure 12. Reduced frequency plot for the storage and loss moduli of the star 4SI-3. The reference temperature was 383 K. The marked data correspond to the temperatures (●) 428, (⊖), 423, (⏀) 418, and (◒) 413 K. Below the frequencies ω_1 and ω_2 the shifted data show one of the limiting slopes: 2 or 0.33.

ω_2 we can study the time evolution of the moduli for over 2 decades in magnitude. The results of the kinetic studies for the asymmetric linear diblock AS25 are shown in Figure 13a. The sample was first heated to an initial temperature T_i = 393 K, located 8 K above the T_{ODT} and then quenched to different final temperatures below the ODT: 379, 380, 381, 382, and 383 K and the evolution of G' and G'' was monitored at a frequency of 1 rad/s. The strain amplitude was kept to ~2% during these studies. Both moduli exhibit a sigmoidal shape which signifies the transformation of the undercooled disordered to the ordered phase. Clearly, this mechanism is T dependent, but there is considerable slowing of the kinetics for the deeper quenches.

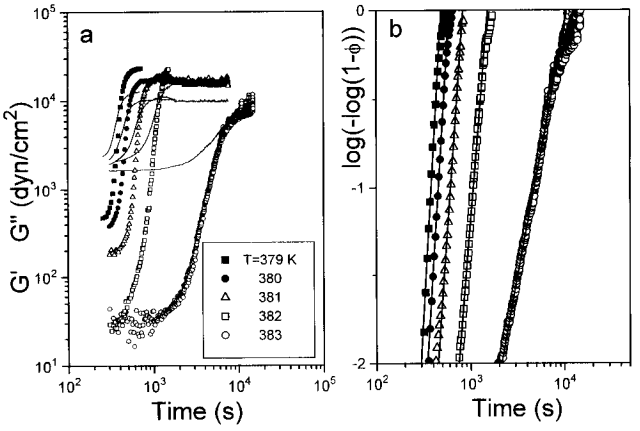

Figure 13. (a) Time evolution of G' (symbols) and G'' (lines) for the asymmetric linear diblock AS25 following a quench from the disordered phase (T_i = 393 K) to different temperatures below the T_{ODT} (=385 K) as indicated. (b) Avrami plots for the volume fraction of the ordered phase $\phi(t)$. Solid lines are fits to the Avrami equation (see text).

To extract the shape and the characteristic time from the data shown in Figure 13a, we have used two appropriate mechanical models as described in detail elsewhere.[47] Briefly, the system is regarded as a composite material made of two phases: a disordered phase at short times and an ordered phase at longer times. The transformation from one phase to the other with time is causing the S shape of the dynamic mechanical response. The viscoelastic properties of composite materials can be very complex and depend on the details of the topology. Here, to extract the volume fraction of the ordered phase ϕ(t), we are using some simple dynamic mechanical models ("series" and "parallel") of the constituent phases.[47] In the "series" model the stresses in the system are uniform, and the contributions of the two phases to the compliance J* should be additive:

$$J^* = (1 - \phi)J_0 + \phi J_\infty \qquad (19)$$

whereas in the "parallel" model the strains are uniform and the contribution to G^* should be additive:

$$G^* = (1 - \phi)G_0 + \phi G_\infty \qquad (20)$$

where J_0 (G_0) and J_∞(G_∞) are the compliances (moduli) of the disordered and ordered phases, respectively. In the present study we are using both models which provide an upper and a lower bound for the $\phi(t)$. The time dependencies of the volume fraction of the ordered phase ϕ, obtained from the two models, are analyzed independently by fitting the Avrami equation:[48]

$$\phi(t) = 1 - \exp(-zt^n) \qquad (21)$$

where z is the rate constant, and n is the Avrami exponent. From the former, the characteristic time for the ordering process can be calculated as $(\ln 2/z)^{1/n}$. Typical Avrami plots using the parallel model are shown

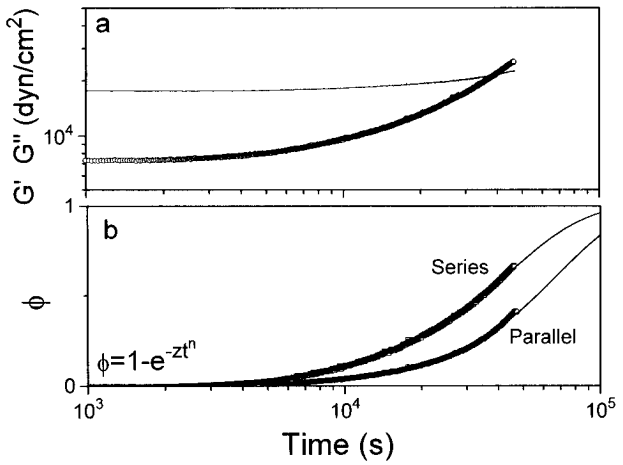

Figure 14. (a) Time evolution of G' and G'' for the star 4SI-3, at $T = 415$ K, following a quench from the disordered phase ($T_i = 433$ K). (b) Time evolution of the volume fraction of the ordered phase calculated using the "series" and "parallel" models (see text). The solid lines are fits to the Avrami equation.

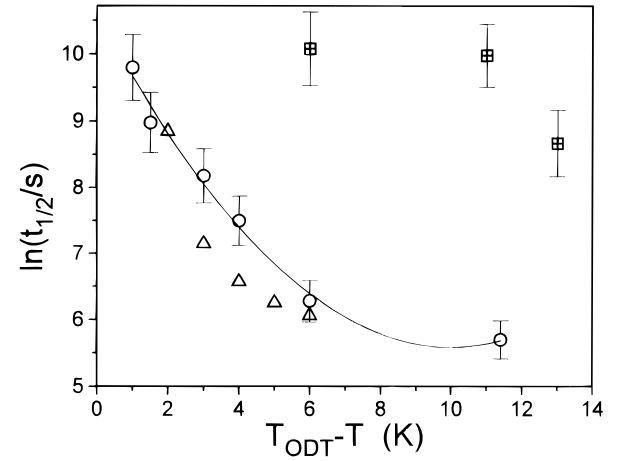

Figure 15. Characteristic ordering times $t_{1/2}$ plotted vs the temperature difference from T_{ODT}, for three block copolymers: (○) SI-85/65 symmetric diblock ($\bar{M}_w = 12\,200$, $f_{PS} = 0.51$), (△) AS25 asymmetric diblock, and (⊞) 4SI-3 star diblock.

also in Figure 13b for the AS25. In agreement with previous investigations[24,14] on linear and graft copolymers, there is a change in slope (implying a change in the Avrami exponent) in going from shallow ($T - T_{ODT} = 3$ K) to deeper quenches. This change of slope—which is beyond the scope of the present study—has been attributed to a change in the mechanism of ordering.[14,24] The ordering kinetics have also been studied in the star diblock 4SI-3 following a quench from the disordered phase ($T_i = 433$ K) to different temperatures in the ordered phase: 420, 415, and 413 K. Figure 14 gives the calculated ϕ(t) from the G' and G'' data, at $T = 415$ K, using the "series" and "parallel" models. Solid lines through the data points are fits to the Avrami equation resulting in an exponent $n = 2$. The characteristic kinetic times are compared in Figure 15 for the linear diblock AS25 and for the star diblock 4SI-3. For comparison, the ordering times from a linear but symmetric diblock copolymer (SI-85/65, $\bar{M}_w = 12\,200$, $f_{PS} = 0.51$) are also plotted.[24] In comparing the characteristic kinetic times between the asymmetric and symmetric linear diblocks, we find that under the same undercooling (fixed $T_{ODT} - T$) the former times are faster by almost half a decade, notwithstanding the higher molecular weight for the asymmetric diblock. This can be

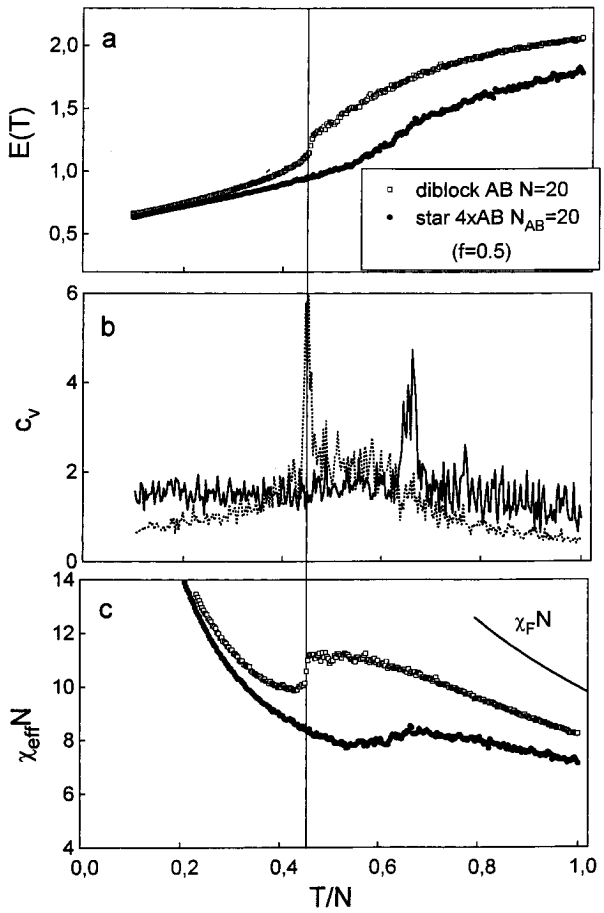

Figure 16. Temperature dependencies of various thermodynamic parameters for a symmetric diblock copolymer (open symbols) with $N = 20$ and a symmetric star diblock (filled symbols) with $N_{AB} = 20$: (a) average interaction energy per monomer, (b) specific heat determined using eq 27 (dashed and full lines correspond to open and filled symbols, respectively), and (c) the effective interaction parameter per chain. The temperature coordinate is normalized by chain length ($N = 20$). The vertical line indicates the temperature where the microphase separation in the linear diblock takes place.

qualitatively understood in terms of a recent droplet model for homogeneous nucleation in diblock copolymers.[49] The model describes the nucleation and subsequent growth of lamellar phases from a supercooled disordered phase. Recently, the model has been extended to include asymmetric diblocks.[50] The theory treats ideal (monodisperse) diblocks and provides the barriers for homogeneous nucleation, for the symmetric case

$$\beta\Delta F_s^* \approx \bar{N}^{-1/3}\delta^{-2} \tag{22}$$

and for the asymmetric case

$$\beta\Delta F_{AS}^* \approx \bar{N}^{1/2}\delta^{-2}|f - 0.5|^5 \tag{23}$$

In equations above, $\beta = 1/kT$, $\bar{N}^{-1/3}$ is the fluctuation correction term and δ ($=\chi - \chi_{ODT}/\chi_{ODT}$) is the undercooling parameter with χ and χ_{ODT} being, respectively, the values of the interaction parameter at the different final temperatures and at the T_{ODT}. Because of the $\bar{N}^{-1/3}$ term, the barrier for symmetric diblocks is expected to decrease with increasing $\bar{N}$. This $\bar{N}$ dependence for the symmetric diblock copolymers has been recently verified experimentally.[23] Alternatively, the barrier for asymmetric diblocks is very large and scales with $\bar{N}^{1/2}$ as with polymer blends. The characteristic

time is related to the nucleation barrier by

$$t_{1/2} \approx \exp(\beta \Delta F^*/4) \tag{24}$$

From eq 24 we can estimate the ratio of the characteristic ordering times in the asymmetric and symmetric cases assuming (i) homogeneous nucleation, (ii) the same prefactors, and (iii) the same undercooling. Using $\bar{N}_{AS} = 2.24\bar{N}_S$:

$$\ln t_{1/2}{}^{AS}/\ln t_{1/2}{}^{S} \approx \sqrt{2.24}\bar{N}_S{}^{5/6}|f - 0.5|^5 \tag{25}$$

and for $\bar{N}_S = 457$, $f = 0.22$ we obtain a value of 0.4 which is in good agreement with the experimental observations in Figure 15. However, the most intriguing feature of Figure 15 is the freezing of the kinetics in the star diblock. Under the same undercooling the star diblock needs about 3 additional decades of time—compared to the equivalent linear diblock—to develop the ordered structure. The difference probably lies in the different architecture. The ordering kinetics in block copolymers are related to the mobility of polymer chains and therefore to the presence of entanglements which can result in the quenching of the star dynamics (through the prefactor of eq 24).

Computer Simulations. We present here results concerning the properties of star and linear copolymer melts over a broad temperature range including both the homogeneous and the microphase-separated state. The simulation provides information on the structure, dynamics, and thermodynamic properties of the systems.[40,51,52] The temperature dependence of some thermodynamic quantities recorded during heating of the initially microphase-separated system are shown in Figures 16 and 17 for the symmetric and asymmetric case, respectively.

The following quantities have been determined: (1) the energy of interaction of a monomer E_m, determined as the average of interactions of all monomer pairs at a given temperature:

$$E_m = \sum_{i=1}^{z} \epsilon_{kl}(i) \tag{26}$$

(2) the specific heat, calculated via the fluctuation–dissipation theorem:

$$c_v = (\langle E^2 \rangle - \langle E \rangle^2)/k_B T^2 \tag{27}$$

where the brackets denote averages over the energy of subsequent states sampled during simulation of the system at constant temperature, and (3) the effective interaction parameter characterized by

$$\chi_{eff} = {}^1/_2\langle E_m \rangle/k_B T \phi_A \phi_B \tag{28}$$

where ϕ_A and ϕ_B are volume fractions of monomers of type A and B, respectively.

In the case of the symmetric diblock (Figure 16), for T/N below 1, the effective energy of interaction decreases and a first-order phase transition, attributed to the microphase separation, is observed at $T/N \approx 0.45$. The jump in the interaction energy at this temperature is accompanied by a sharp peak in the specific heat (Figure 16b). Changes in the interaction energy are caused by two effects. At high temperatures, it is the intramolecular distribution of monomers which affects the interaction energy. At low temperatures, there are additional contributions from morphological effects related to the process of microphase separation. The dependence of the same quantities determined for the star molecules in the simulated melt are similar in nature but differ quantitatively. Already at high temperature ($T/N = 1$) the interaction energy of star block copolymers is considerably smaller than for the linear diblock. This is due to additional intramolecular correlations resulting from the junction between identical blocks in the center of the star. This effect of the intramolecular *preseparation* of different monomers results in a higher temperature of the microphase separation of the whole system. The symmetric star block system has the same morphology as the symmetric diblock (lamellar) which results in a similar interaction energy of the two systems at low temperatures. The values of the effective interaction parameters $\chi_{eff}N$ for the two systems in the vicinity of the ODT are considerably different. They are 11 and about 8 for linear and star chains, respectively, in good agreement with the theoretical predictions (Figure 4).

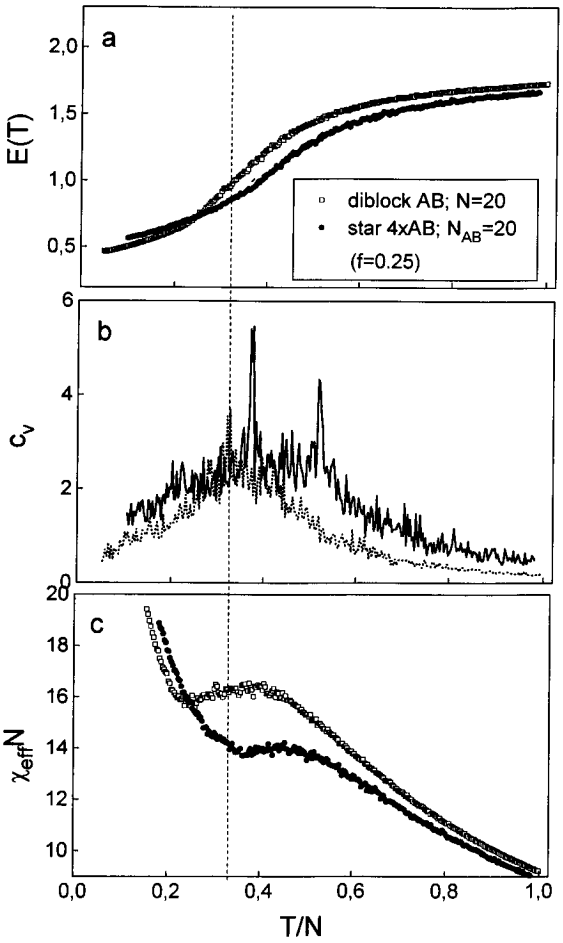

Figure 17. Temperature dependencies of various thermodynamic parameters for an asymmetric diblock copolymer (open symbols) ($N = 20$, $f = 0.25$) and an asymmetric star diblock (filled symbols) ($N_{AB} = 20$, $f = 0.25$): (a) average interaction energy per monomer, (b) specific heat determined using eq 27 (dashed and full lines correspond to open and filled symbols, respectively), and (c) the effective interaction parameter per chain. The temperature coordinate is normalized by the chain length ($N = 20$). The vertical dashed line indicates the temperature where the microphase separation in the linear diblock takes place.

Similar effects are observed when asymmetric star block polymers are compared with the corresponding linear polymer (Figure 17). The connectivity of the diblock arms into the star results in higher tempera-

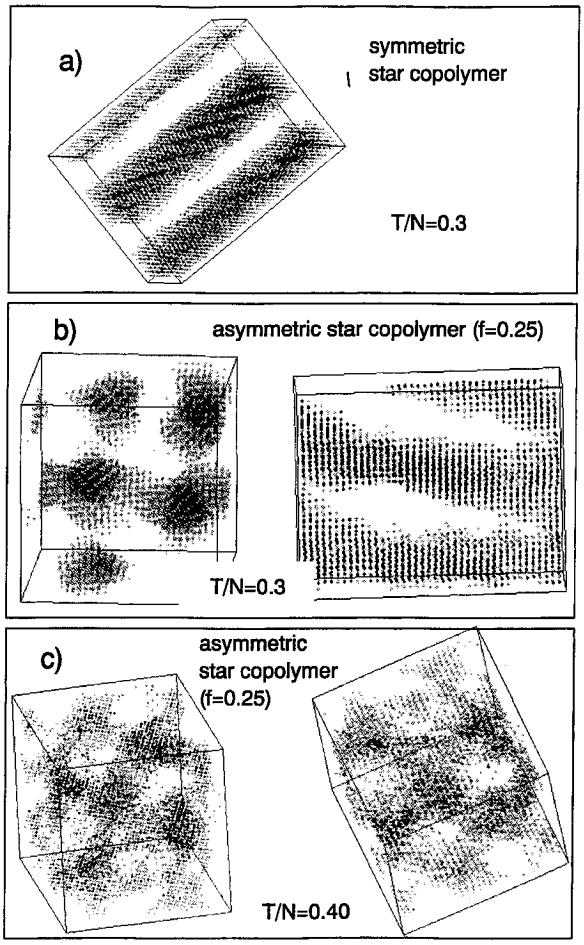

Figure 18. Projections of various models of star copolymers equilibrated at temperatures corresponding to the microphase-separated states. In all cases monomers of one component only are shown. In the case of the asymmetric star copolymers, it is the minor component which is shown. The orientation of models is chosen in such a way that the type of morphology is well visible: (a) lamellar structure formed below the T_{ODT} in the symmetric star copolymer system, (b) two projections of the system with asymmetric star copolymers illustrating the cylindrical microdomain morphology, and (c) the lower-T intermediate phase of the asymmetric star block copolymer with the bicontinuous cubic structure illustrated by two different projections of the model equilibrated at $T/N = 0.4$, i.e., slightly above the transition to the cylindrical morphology.

tures of the microphase separation and in lower effective interaction parameter ($\chi_{eff}N$) at the transition. The asymmetric copolymer stars undergo multiple transitions which are related to the different morphologies in the microphase separated state (Figure 4). The high-T transition ($T/N \approx 0.52$) separates the disordered state and a microphase-separated state with spherical microdomains of the minor component, and the low-temperature transition ($T/N \approx 0.37$) is a transition to the cylindrical morphology. Both transitions take place at higher temperatures than for the linear chains ($T/N = 0.32$). The decrease of the effective interaction parameter of stars with respect to that of linear chains is in good agreement with the theoretical predictions as well as with the experimental results (Figure 8). At the two transitions for the asymmetric stars the $\chi_{eff}N$ was nearly the same and equal to $\approx$14, whereas, for the linear chains the value $\chi_{eff}N = 16.4$ was obtained.

The morphologies observed in the simulated systems, at various states corresponding to different temperatures, are presented in Figure 18. In the symmetric star copolymer a well-ordered lamellar microstructure is observed below T_{ODT} (Figure 18a). In the asymmetric star copolymer the lowest temperature morphology ($T/N = 0.3$) corresponds to cylindrical microdomains which are shown in Figure 18b, at two projections. The higher T cubic structure resembles a bcc also found in the experiment, but at lower T, near the low-T peak in the specific heat a bicontinuous cubic structure is formed (Figure 18c). Extra effort has been undertaken in identifying the coordination of the channel-forming minority phase by connecting lines between neighboring beads. This procedure revealed that the channels are devided into two interpenetrating phases and have a 3-fold coordination. The identification was not easy, but the outcome resembles more the gyroid phase in agreement with the theoretical predictions. It is the first time, to our knowledge, that such bicontinuous cubic structures have been seen in computer simulations. In a future work we will examine the finite-size effect of the system on the ordered phases.

Conclusion

Theory, computer simulations, and experiment have been employed to study the phase behavior and the order−disorder transition in four-arm star diblock copolymers of styrene and isoprene. The theoretical approach which is based on the higher harmonics predicts a stable gyroid phase over a limited composition range. Fluctuation corrections have been calculated and shown to affect mainly the bcc and hexagonal phases. The computer simulations of asymmetric four-arm star diblocks revealed the following succession of phases on heating: hexagonal − bicontinuous cubic − bcc − disordered. The bicontinuous cubic phase has a 3-fold coordinated structure similar to the gyroid phase. In the experiment the order−disorder transition and the ordering kinetics have been investigated by SAXS and rheology. Both techniques were used to obtain the T_{ODT} and the mean-field structure factor was used to describe the SAXS profiles at $T \gg T_{ODT}$. The weak $\chi(T)$ restricts the exploration of the phase diagram to a small region where spherical microdomains of PS are organized in a bcc lattice. The ordering kinetics have been studied by rheology and revealed a slowing of the ordering process as compared to linear diblocks as a result of the molecular topology and constrained mobility of chains.

Acknowledgment. G.F. acknowledges the support of the Alexander von Humboldt Foundation for a grant (FOKOOP).

References and Notes

(1) Leibler, L. *Macromolecules* **1980**, *13*, 1602.
(2) Fredrickson, G. H.; Helfand, E. *J. Chem. Phys.* **1987**, *87*, 697.
(3) Erukhimovich, I. Ya.; Dobrynin, A. V. *Macromol. Symp.* **1994**, *81*, 253.
(4) Olvera de la Cruz, M.; Mayes, A. M.; Swift, B. W. *Macromolecules* **1992**, *25*, 944.
(5) Förster, S.; Khandpur, A. K.; Zhao, J.; Bates, F. S.; Hamley, I. W.; Ryan, A. J.; Bras, W. *Macromolecules* **1994**, *27*, 6922; Khandpur, A. K., Förster, S.; Bates, F. S.; Hamley, I. W.; Ryan, A. J.; Bras, W.; Almdal, K.; Mortensen, K. *Macromolecules* **1995**, *28*, 8796.
(6) Hajduk, D. A.; Harper, P. E.; Gruner, S. M.; Honeker, C. C.; Thomas, E. L.; Fetters, L. J. *Macromolecules* **1995**, *28*, 2570.
(7) Matsen, M. W.; Schick, M. *Macromolecules* **1994**, *27*, 4014.
(8) Erukhimovich, I. Ya. *Vysokomol. Soedin* **1982**, *A24*, 1950 (translated in *Polym. Sci. USSR (Engl. Transl.)* **1982**, *24*, 2232).
(9) Olvera de la Cruz, M.; Sanchez, I. C. *Macromolecules* **1986**, *19*, 2501.
(10) Mayes, A. M.; Olvera de la Cruz, M. *J. Chem. Phys.* **1989**, *91*, 7228.

(11) Benoit, H.; Hadziioannou, G. *Macromolecules* **1988**, *21*, 1449.
(12) Dobrynin, A. V.; Erukhimovich, I. Ya. *Vysokomol. Soedin.* **1990**, *B22*, 663 (in Russian).
(13) Dobrynin, A. V.; Erukhimovich, I. Ya. *Macromolecules* **1993**, *26*, 276.
(14) Floudas, G.; Hadjichristidis, N.; Iatrou, H.; Pakula, T.; Fischer, E. W. *Macromolecules* **1994**, *27*, 7735.
(15) Fetters, L. J.; Richards, R. W.; Thomas, E. L. *Polymer* **1987**, *28*, 2252.
(16) Hashimoto, T.; Ijichi, Y.; Fetters, L. J. *J. Chem. Phys.* **1988**, *89*, 2463.
(17) Ijichi, Y.; Hashimoto, T.; Fetters, L. J. *Macromolecules* **1989**, *22*, 2817.
(18) Archer, L. A.; Fuller, G. G. *Macromolecules* **1994**, *27*, 4804.
(19) Johnson, J. M.; Allgrair, J. B.; Wright, S. J.; Young, R. N.; Buzza, M.; McLeish, T. C. B. *J. Chem. Soc., Faraday Trans.* **1995**, *91*, 2403.
(20) Morton, M.; Fetters, L. *J. Rubber Chem. Technol.* **1975**, *48*, 359.
(21) Iatrou, H.; Hadjichristidis, N. *Macromolecules* **1993**, *26*, 2479.
(22) Winter, H. H.; Scott, B. D.; Gronski, W.; Okamoto, S.; Hashimoto, T. *Macromolecules* **1993**, *26*, 7236.
(23) Floudas, G.; Vlassopoulos, D.; Pitsikalis, M.; Hadjichristidis, N.; Stamm, M. *J. Chem. Phys.* **1996**, *104*, 2083.
(24) Floudas, G.; Pakula, T.; Fischer, E. W.; Hadjichristidis, N.; Pispas, S. *Acta Polym.* **1994**, *45*, 176.
(25) Dobrynin, A. V.; Erukhimovich, I. Ya. *Vysokomol. Soedin.* **1990**, *B32*, 852 (in Russian).
(26) Landau, L. D. *Zh. Exp. Theor. Fiz.* **1937**, *7*, 627.
(27) Alexander, S.; Mc Taque, J. *Phys. Rev. Lett.* **1978**, *41*, 702.
(28) de Gennes, P.-G. *Faraday Discuss. Chem. Soc.* **1979**, *68*, 96.
(29) Erukhimovich, I. Ya. *Vysokomol. Soedin.* **1982**, *A24*, 1942 (translated in *Polym. Sci. USSR (Engl. Transl.)* **1982**, *24*, 2223).
(30) Brazovskii, S. A. *Zh. Exp. Theor. Fiz., Sov. Phys. JETP* **1975**, *68*, 175.
(31) Dobrynin, A. V.; Erukhimovich, I. Ya. *J. Phys. II (Fr.)* **1991**, *1*, 1387.
(32) Dobrynin, A. V.; Erukhimovich, I. Ya. *Vysokomol. Soedin.* **1991**, *A33*, 1100 (translated in *Polym. Sci. USSR (Engl. Transl.)* **1992**, *33*, 1012).
(33) Mayes, A. M.; Olvera de la Cruz, M. *Mater. Res. Soc. Proc.* **1990**, *175*, 345.
(34) Mayes, A. M.; Olvera de la Cruz, M. *J. Chem. Phys.* **1991**, *95*, 4670.
(35) Thomas, E. L.; Alvard, D. B.; Kinning, J. J. *Macromolecules* **1986**, *19*, 2197.
(36) Marques, C. M.; Cates, M. E. *Europhys. Lett.* **1990**, *13*, 267.
(37) Erukhimovich, I. Ya., to be published.
(38) Matsen, M. W.; Schick, M. *Phys. Rev. Lett.* **1994**, *72*, 2660.
(39) Matsen, M. W.; Schick, M. *Macromolecules* **1994**, *27*, 6761.
(40) Floudas, G.; Vogt, S.; Pakula, T.; Fischer, E. W. *Macromolecules* **1993**, *26*, 7210.
(41) Roovers, J. E. L.; Bywater, S. *Macromolecules* **1972**, *5*, 385.
(42) Hadjichristidis, N.; Roovers, J. E. L. *J. Polym. Sci., Polym. Phys. Ed.* **1974**, *12*, 2521.
(43) Floudas, G.; Fytas, G.; Hadjichristidis, N.; Pitsikalis, M. *Macromolecules* **1995**, *28*, 2359.
(44) Rubinstein, M.; Obukhov, S. P. *Macromolecules* **1993**, *26*, 1740.
(45) Floudas, G.; Hadjichristidis, N.; Iatrou, H.; Avgeropoulos, A.; Pakula, T., submitted to *Macromolecules*.
(46) Rosedale, J. H.; Bates, F. S. *Macromolecules* **1990**, *23*, 2329.
(47) Ferry, J. D. In *Viscoelastic Properties of Polymers*, 3rd ed.; Wiley and Sons: New York, 1980.
(48) Avrami, M. J. *J. Chem. Phys.* **1939**, *7*, 1103; **1940**, *8*, 212; **1941**, *9*, 177.
(49) Fredrickson, G. H.; Binder, K. *J. Chem. Phys.* **1989**, *91*, 7265.
(50) Binder, K. *Physica* **1995**, *A213*, 118.
(51) Gauger, A.; Pakula, T. *Macromolecules* **1995**, *28*, 190.
(52) Vilesov, A. D.; Floudas, G.; Pakula, T.; Melenevskaya, E. Yu.; Birshtein, T. M.; Lyatskaya, Y. V. *Macromol. Chem. Phys.* **1994**, *195*, 2317.

MA951762V